https://doi.org/10.5194/egusphere-2026-6547
Preprint. Discussion started: 30 October 2026
© Author(s) 2026. CC BY 4.0 License.

The contribution of mesoscale dynamics to the tropical anvil cloud growth rate

Rémy Roca[1], Thomas Fiolleau[1], Léna Arthur[1], Nathanaël Asfaw[1], Cathy Hohenegger[2], Gregory S. Elsaesser[3], Caroline J. Muller[4], Jean-Pierre Chaboureau[5] and Romain Fiévet[2].

1 Université de Toulouse, Laboratoire d'Etudes en Géophysique et Océanographie Spatiales (CNRS/CNES/IRD/UPS), Toulouse, France

2 Max Planck Institute for Meteorology, Hamburg, Germany

3 NASA GISS and Columbia University, New York, New York, USA

4 Institute of Science and Technology Austria ISTA, Klosterneuburg, Austria

5 Université de Toulouse, CNRS, IRD, LAERO, Toulouse, France

Correspondence to: Rémy Roca (remy.roca@cnrs.fr); ORCID: 0000-0003-1843-0204

Abstract. Tropical anvil cloud life cycle remains a strong source of uncertainty in our understanding of the ice cloud climate feedback. From an object-oriented perspective, the anvil cloud shield of convective systems exhibits a well documented growth and a decay phase. This study focuses on the less understood processes at play in the growing phase. Radiative convective equilibrium (RCE) numerical experiments from km-scale models and a cloud tracking algorithm are used together with an analytical budget equation to decipher the various contributions to the anvil area growth rate. It is first shown that anvil growth rates in the RCE simulations are consistent with satellite observations-derived anvil properties, confirming the fitness for purpose of these simulations. Then, the Minimal ANvil growTh Analytic (MANTA) model for anvil growth rate is introduced. It links the growth rate to the detrainment of cloudy air and a simple cloud sink. The minimal model is shown to perform very well in explaining the simulated growth rates. Following a mechanism denial approach, the minimal model shows that both the convective and non convective, i.e. mesoscale, vertical motions, have to be considered to predict the correct growth rate. The growth rate is balanced by a source term due to overall detrainment, which is three to four times larger than the sink term, depending on the km-scale model used. These relative contributions are furthermore shown to be constant across the whole range of growth rates for all of the simulations.

https://doi.org/10.5194/egusphere-2026-6547
Preprint. Discussion started: 30 October 2026
© Author(s) 2026. CC BY 4.0 License.

Introduction

Cirrus clouds over the tropical belt are important to the Earth radiation budget by reflecting part of the incoming shortwave radiation and by absorbing longwave radiation (Stephens et al., 2024). The thicker cirrus are thought to have a cooling to neutral effect on the top of the atmosphere radiative budget while thinner cirrus have a net warming effect (Gasparini et al., 2025). These ice clouds can be related to in-situ formation processes or to deep convective origin (Mu et al., 2025). The latter are often termed anvil cirrus. The climatology of anvil cirrus exhibits a top-heavy vertical profile with a peak in the upper troposphere where the maximum convective detrainment occurs (Stephens et al., 2008). Anvil cirrus results from deep convection that first detrains cloudy air in the upper troposphere where the cloud material then spreads and eventually dissipates. This anvil life cycle is accompanied by changes of the cloud radiative properties and has been identified as an important element of the overall tropical high cloud effect on the radiative budget of the tropics (Hartmann and Berry, 2017; Lutsko et al., 2026).

Anvil cloud life cycle can be apprehended following an object-oriented approach by considering individual cloud systems. In such cloud systems, anvil cloud corresponds to the *cumulonimbus incus* directly attached to deep convection (Hartmann et al., 2018; Houze, 1993). Using a view-from-above geometry, readily available from a meteorological satellite perspective, the cloud systems appear as individual cloud clusters. We refer to these clusters as the cloud shield of deep convective systems (DCS) (Houze, 2004). The DCS cloud shield is usually delineated using thermal infrared imagery. In terms of brightness temperature, the cluster appears as a cold structure with a very cold core surrounded by a slightly warmer area (Maddox, 1980). In the coldest part, deep convection is active and ice loading is high, and the column acts as a black body from which upwelling infrared radiation emanates near cloud top at upper tropospheric temperatures. The warmer part corresponds to the anvil and it is less optically thick than the convective part and slightly departs from the black body. The upwelling radiation hence combines emission from the cloud top temperature and contribution from lower level in the troposphere, resulting in a warmer brightness temperature (Roca and Ramanathan, 2000). The detection of the thinner part of the anvil is hence difficult due to the possible influence of underlying low level cloud features (Bouniol et al., 2016). To prevent misassociation, the DCS cloud shields are usually restricted to the thicker part of the anvil (IWP > 200-300 g m-2), where the attribution is unambiguous, using cold thresholds in the infrared imagery (Fiolleau and Roca, 2013). These cloud shields span a large spectrum of spatial extension, duration and morphology (Fiolleau and Roca, 2024). Despite complex internal dynamical and microphysical processes coupling deep convection to the system's cloud shield, the life cycle of the resulting cloud shield is characterized by a simple pattern, consisting of a growing and a decaying phase, where the area of the shield first grows and then shrinks linearly (Roca et al., 2017).

The decaying phase of the cloud shield starts when the dissipation term dominates the cloud production budget. Using a satellite observation informed source-sink model, Elsaesser et al., (2022) estimated that the individual thick anvil cloud shield starts shrinking when the fraction

https://doi.org/10.5194/egusphere-2026-6547
Preprint. Discussion started: 30 October 2026
© Author(s) 2026. CC BY 4.0 License.

of active convection is less than 15% of the anvil cluster. The processes controlling the cloud sink and its lifetime parameter that dominates the decaying phase have been extensively investigated. Lilly (1988) introduced a two stage model of anvil cirrus extension and dissipation. The first stage is short and concerns the spreading and thinning of buoyant air from convection into a stable upper tropospheric layer. The following stage lasts longer and relates the anvil cirrus layer to a radiative convective mixed layer driven by vertical heating gradients. Precipitation (or sedimentation) and microphysical processes are also important to the decay time of the anvil (Gasparini et al., 2023a). Microphysics can act both as a source (growth/deposition, nucleation by turbulent mixing) or a sink (sublimation) of anvil ice (Seeley et al., 2019). The vertical heating gradient in the anvil layer not only favors convective instability (Ackerman et al., 1988) but also gives rise to a mesoscale lifting that contributes to sustain the anvil life cycle (Hartmann et al., 2018; Wall et al., 2020).

While the suite of processes involved in the dissipation phase of anvil cloud is well identified, comparatively, much less is known about the processes involved in the growing phase of the cloud shield despite its importance in actually setting the initial condition for the decaying phase and consequently for the thick anvil cloudiness as a whole. In the growing phase, cloud production is larger than the dissipation term. In this phase, the role of the latent heating due to convective precipitation to the heat budget of the anvil is overwhelming and radiative heating is often neglected (Houze 1982; Houze 2004). Similarly, transport by narrow convective updrafts or convective cores is expected to be the dominant source of detrained cloud materials (Beydoun et al., 2021; Elsaesser et al., 2022; Gasparini et al., 2019, 2023b; Lilly, 1988; Lutsko et al., 2026; Seeley et al., 2019; Takahashi et al., 2017).

In this paper, we show that this convective-centric view is too restrictive and that the detrainment from the full spectrum of vertical motions, including the non-convective, mesoscale circulation, internal to the anvil, needs to be accounted for to fully describe the growth rate during the growing phase of the anvil cloud shield. This result is achieved using a simple analytical model, the Minimal ANvil growTh Analytic (MANTA) model, to provide a physically transparent interpretation of the results of radiative–convective equilibrium (RCE) numerical simulations which are used in combination with a cloud-tracking algorithm. First, the MANTA model is used to quantify the relative contribution of convective scale and mesoscale to the anvil growth rate. Second, it is used to perform mechanism-denial experiments that reveal the role of the non-convective detrainment to the anvil cloud production.

Our study uses numerical simulations that follow the protocol of the Radiative–Convective Equilibrium Model Intercomparison Project (Wing et al., 2018). Such an idealized framework is an important component of the hierarchical modeling approach, which has proven particularly valuable for understanding climate processes and their underlying mechanisms (Maher et al., 2019). In addition to previous bulk analyses of convection–climate interactions in these simulations (Wing et al., 2020), we here perform statistical analysis of the growth phase from a large number of individual convective systems obtained by a cloud-tracking algorithm applied to 25 days of simulations. Process-oriented analysis of thousands of

https://doi.org/10.5194/egusphere-2026-6547
Preprint. Discussion started: 30 October 2026
© Author(s) 2026. CC BY 4.0 License.

individual systems is complementing previous studies that have primarily relied on more classical single convective system case-study approaches. Furthermore, three different kilometer scale models are used to account for uncertainties and diversity in the representation of microphysical processes, which have been shown to strongly influence the life cycle and properties of anvil clouds (Fan et al., 2017; Hartmann et al., 2018).

The paper is structured as follows. Section 2 provides a detailed description of the simulations and their processing using the cloud-tracking algorithm. The simulated growth rates are then compared against satellite observations. Section 3 introduces the MANTA model and its application to the analysis of simulated cloud growth rates. The sensitivity experiments are also presented in this section. Finally, Section 4 discusses the results and a conclusion and outlook section ends the paper.

Data

The RCEMIP setup and the simulations

The simulations used here are following the RCEMIP protocol for a Cloud Resolving Model with a 300K SST (Wing et al., 2018). All integrations are performed as per the original protocol but with a specific output frequency of 30 min instead of 1-3h and the use of instantaneous fields to accommodate the cloud tracking algorithm. The integration lasts 100 days and the last 25 days only are used and analyzed here to remove spin-up effects (Wing et al., 2020).

The cloud-resolving model System for Atmospheric Modeling (SAM) is used (Khairoutdinov and Randall, 2003), using the same version (6.11.2) and settings as the one that participated in the original RCEMIP exercise. In particular, we used the Rapid Radiative Transfer Model (Mlawer et al., 1997) for radiation, the MPDATA advection scheme, the default SAM1MOM one moment microphysical scheme, and the TKE subgrid-scale closure (stationary Smagorinsky scheme). The model SAM solves the anelastic conservation equations for momentum, mass, energy, and water, which is present in the model in six species (water vapor, cloud liquid, cloud ice, rain, snow and graupel). The upper third of the domain (18-27 km) has a sponge layer to absorb gravity waves, which would otherwise unrealistically fill our doubly-periodic domain. The grid spacing is 3 km in both horizontal directions, and increases with height, starting at a few tens of meters in the planetary boundary layer, and increasing to 500 m in the mid and upper troposphere.

Meso-NH (MNH thereafter) version 5.4.2 (Lac et al., 2018) employs the anelastic equation set on a fully staggered Cartesian Arakawa-C grid. The dynamics packages include a 4th-order centered advection scheme for momentum variables and a piecewise parabolic method scheme for other variables. The physics packages include the two-stream scheme for shortwave radiation (Fouquart, Y. and Bonnel, B., 1980), the Rapid Radiative Transfer Model (Mlawer et al., 1997) for longwave radiation, the 1.5 order closure turbulent kinetic energy scheme (Cuxart et al., 2000) with a mixing length parameterisation (Bougeault and Lacarrere,

https://doi.org/10.5194/egusphere-2026-6547
Preprint. Discussion started: 30 October 2026
© Author(s) 2026. CC BY 4.0 License.

1989), the single-moment mixed microphysics scheme (Pinty, J.-P. and P. Jabouille, 1998), and an eddy diffusivity mass flux scheme for shallow convection (Pergaud et al., 2009). The horizontal grid spacing is 3 km. The model top is at 33 km with 76 vertical levels spaced 500 m apart above 3 km. This is the same version of the model as the one that participated in the original RCEMIP exercise.

The third model is the new ICOsahedral Nonhydrostatic (ICON) model in its Sapphire configuration (Hohenegger et al., 2023), based on the ICON model version 2.6.5. The model solves the nonhydrostatic version of the Navier-Stokes equations together with the conservation laws for mass and energy. The equations are discretized on an icosahedral-triangular C-grid. The Sapphire configuration only retains a parameterization for radiation, using the Radiative Transfer for Energetics RRTM for General circulation model applications-Parallel (RTE-RRTMGP) scheme (Pincus et al., 2019), and for turbulence, using the Smagorinsky scheme (Lilly, 1962; Smagorinsky, 1963), and for microphysics (Baldauf et al., 2011) a one-moment scheme predicting water vapor, cloud water, rain, cloud ice, snow and graupel. A Rayleigh damping layer is used above 22.5 km with a Rayleigh coefficient of 0.1 s-1. The horizontal grid spacing is 3 km. We use 75 stretched vertical levels with a model top at 33 km.

Identification of individual convective system cloud shield

The TOOCAN algorithm

The TOOCAN algorithm identifies and tracks DCSs from thermal infrared brightness temperature (BT) fields using a three-dimensional spatio-temporal segmentation (Fiolleau and Roca, 2013). This framework enables a consistent characterization of the full life cycle, spatial extent, and cloud-top properties of individual convective systems. It is free of split and merge artefacts and was shown to provide a physically consistent life cycle of the cloud shield of DCS (Elsaesser et al., 2022; Roca et al., 2017). Although originally developed for satellite observations, TOOCAN was here adapted for use with simulated convection fields. DCS identification proceeds iteratively from 190 K to 235 K in 2 K steps. At each step, seeds detected at the current threshold, if any, are spread to neighboring pixels up to 2 K warmer using a 10-connected spatio-temporal operator. This detect-and-spread operation is repeated at each successive threshold until 235 K is reached, which defines the outer edge of the DCS cloud shield. Convective pixels that do not satisfy the minimum tracking criteria, in terms of spatial contiguity or temporal persistence, remain unclassified and are excluded from the DCS population. Following Roca et al., (2017), the systems are partitioned into two classes: short-lived systems, under 2.5 hours for which no life cycle can be extracted at the 30 minutes resolution, and longer-lived systems. In this work only the longer-lived systems are considered.

https://doi.org/10.5194/egusphere-2026-6547
Preprint. Discussion started: 30 October 2026
© Author(s) 2026. CC BY 4.0 License.

Satellite observations

The TOOCAN database (Fiolleau and Roca, 2024) is used to evaluate the simulations. The database relies on geostationary satellite thermal infrared observations over the 2012-2020 period. Satellite BTs are intercalibrated and corrected for zenith angle–dependent limb cooling, which artificially reduces brightness temperatures at large viewing angles (Fiolleau et al., 2020). This correction removes geometry-induced biases in cloud-top temperatures and ensures consistency with model-based diagnostics. A 30 minute time step is used to run the TOOCAN algorithm and to compute the DCS's duration and maximum extension.

Simulation outputs

OLR from the simulations is first converted into BT in the geostationary window channel using the Meteosat-5 spectral response to mimic the observations. For realistic simulations such conversion relies on an observed relationship (Feng et al., 2025) but for the current RCE set ups the relationship has to be reevaluated. The procedure consists of using a subset of the simulations and the RTTOV-13 radiative transfer model (Geer et al., 2021; Saunders et al., 2018) and regressing the OLR onto the Meteosat-5 simulated brightness temperature as detailed in Bolot et al. (2025) for the SAM simulations. Here the same procedure has been performed independently for MNH and ICON simulations. The TOOCAN algorithm is applied to simulation outputs at 30-minute temporal resolution consistent with the satellite observed database. The doubly periodic domain, and cyclic boundary conditions are carefully handled by replicating the simulations and building a larger field ensuring continuity of DCS cloud shields across domain edges and avoiding artificial fragmentation or double counting. As for the observational analysis, the threshold of 235K is used to delineate the thick anvil cloudiness and the edges of the cloud shield.

Model	Total thick anvil (BT<235K)	Unclassified	Short lived	DCS
	Coverage (% of total # of pixels)	Contribution to coverage	Contribution to coverage	Contribution to coverage
SAM	3.2 %	14.3 %	0.1 %	85.6 %
MNH	4.8 %	4.0 %	< 0.1 %	96.0 %
ICON	4.4 %	18.4 %	0	81.6 %

Table 1: Statistics of thick anvil coverage and its repartition across the three classes for the three simulations.

The total thick anvil area covers around 4% of the simulated domain during the analyzed 25 days. Analyzing the idealized simulations using the cloud tracking algorithm further reveals that most of the thick anvil cloudiness (>80%) is indeed associated with DCSs (Table 1). This indicates that a large fraction of the thick anvil in the idealized simulations results from convective systems and not "pop corn" or unorganized convection. The statistics of the

https://doi.org/10.5194/egusphere-2026-6547
Preprint. Discussion started: 30 October 2026
© Author(s) 2026. CC BY 4.0 License.

morphology of the DCS cloud shields are illustrated in Figure 1. The three simulations are populated with systems with similarly distributed growth phase durations with a mode around 2h and a tail up to 8h. MNH exhibits more frequently longer lasting systems than the two other models. The most frequent systems are rather small between 800 and 1500km^2 up to 10^4km^2 and ICON slightly under-represents the largest systems (A_{max}> 4000km^2) compared to the other models and over-estimates the frequency of mid-sized systems with A_{max} around 1500km2.

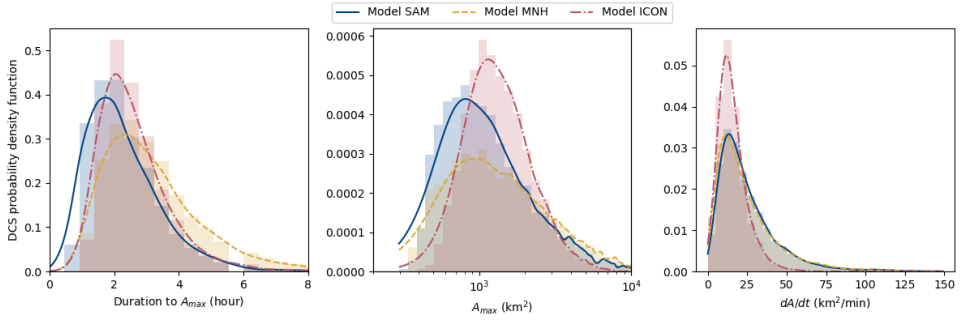

Figure 1: The left panel shows the probability density function of the duration of the growing phase of systems, the middle panel the maximum extension of the DCS during its life cycle and the right panel the growth rate in the growth phase.

In particular, large growth rates are much less frequent in ICON compared to the other models, consistent with a limited ability to reach large shield extensions possibly because of limited convective organization. Possible reasons for this feature relate to deficiencies in the simulated relationship between convective organization and the environment (Wang et al., 2026). More specifically it could also relate to a deficient coupling between convection and humidity shown to control convective organization in some km scale simulations (Takasuka et al., 2024, 2026). More advanced microphysics has also been shown to improve the convective organization compared to the simple scheme used in this version (Waman et al., 2026).

Evaluation of the simulated instantaneous growth rate against satellite observations

Current km-scale climate models, when run in realistic configurations (Stevens et al. 2019), reproduce distributions of the duration and maximum extent of DCS cloud shields that compare well with concurrent satellite observations in the tropics (Prein et al. 2024; Feng et al. 2025). The life cycle of the DCS cloud shield is also reasonably well represented in these simulations (Abramian et al. 2025). The RCE experiments used here are, however, strongly idealized, with a homogeneous surface temperature, channel geometry, no rotation, and no diurnal cycle, and differ substantially from these realistic simulations. This idealized setup

https://doi.org/10.5194/egusphere-2026-6547
Preprint. Discussion started: 30 October 2026
© Author(s) 2026. CC BY 4.0 License.

precludes a direct comparison between our simulations and observations, since the spatial extent of the simulated storms is not directly comparable to that of real DCSs. Instead we focus on the key features of the system's cloud shield growth rate. In particular the linearity of the growth over the whole growth phase can be estimated by computing the standard deviation of the growth rate over the growing phase of the system defined as

$$\sigma_{DCS} = \sqrt{\frac{1}{N}\sum_{i=1}^{N}\left[\left(\frac{dA}{dt}\right)_i - \mu_{DCS}\right]^2}$$

where N is the number of steps of the active phase of the DCS, and μ_{DCS} is the average of the growth rate during the growth phase and reads as

$$\mu_{DCS} = \frac{1}{N}\sum_{i=1}^{N}\left[\left(\frac{dA}{dt}\right)_i\right]$$

The distribution of σ_{DCS} estimated from the satellite record includes ocean-only systems from the TOOCAN database during the 2012 to 2020 period and over the 40°S - 40°N region. Because there is no readily available estimation of the source term from the satellite observation, the active phase is instead approximately delineated by considering the time step of the growth phase where $0.1A_{max} < A < 0.9A_{max}$ which avoids the inclusion of most of the initiation and terminating phases in the computations. We return to these definitions in the next section.

https://doi.org/10.5194/egusphere-2026-6547
Preprint. Discussion started: 30 October 2026
© Author(s) 2026. CC BY 4.0 License.

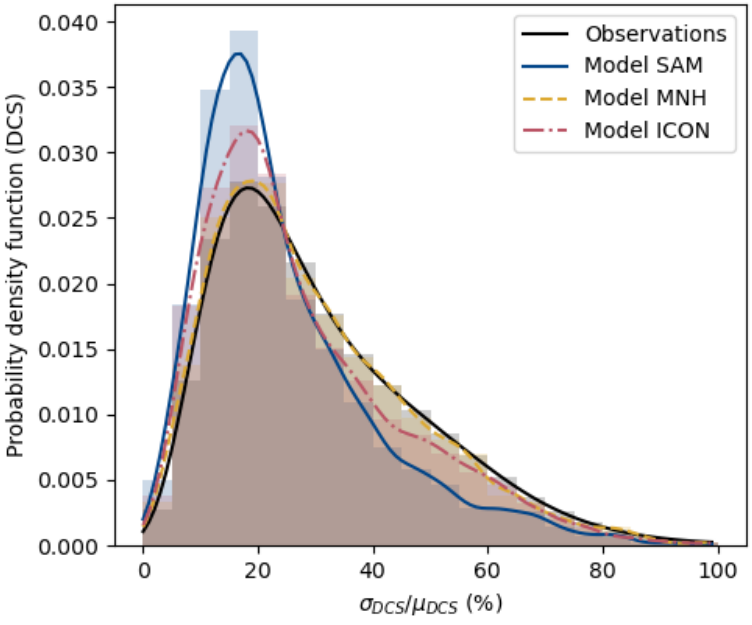

Figure 2: Normalized standard deviation of the growth rate over the growth phase (%) for the three simulations and the observational record. See text for details.

The observation-derived statistics show a distribution peaking at around 20% (Figure 2) indicative of a relatively steady instantaneous growth rate during the entire growth phase, or alternatively a rather linear growth phase (Roca et al., 2017). The three models compare very well to this reference. The simulations tend to have somewhat more frequent smaller normalized standard deviations and less of the largest, compared to the observations, indicating slightly more linear growth in these models than observed. The three simulations exhibit a large diversity of morphological characteristics for their DCS population like duration, maximal extension and growth rate spanning a large phase space (Figure 1). The simulated anvil cloud shield growth rate variability closely resembles the observed one giving us confidence in the ability of these idealized simulations to highlight the relevant physical processes at play.

Identification of deep convective and mesoscale columns

The deep convective columns are identified within the anvil cloud shield using a simplified version of the physical threshold algorithm of Marinescu et al., (2016). The convective columns are first identified by following a suite of tests, based on vertical velocity, above and below the freezing level, the intensity of surface precipitation and cloud top altitude. Only the

https://doi.org/10.5194/egusphere-2026-6547
Preprint. Discussion started: 30 October 2026
© Author(s) 2026. CC BY 4.0 License.

columns within cloud shields are analyzed (BT< 235K). A column is labeled as convective if the surface precipitation exceeds a threshold of 10 mm/h or if the absolute magnitude of vertical velocity, in the updrafts or in the downdrafts, above (resp. below) the 0°C isotherm exceeds 5m s^{-1} (resp. 3m s^{-1}). As such the convective column identification relates to vigorous, likely young convection. These thresholds have been shown to yield a physically sound description of convective organization in km-scale RCE simulations (Netz et al., 2025). Second, the part of the anvil cloud shield that is not identified as convective is labelled as non-convective, termed "mesoscale" later in the manuscript.

A minimal model of the anvil shield growth rate

Formulation

Here we introduce the Minimal ANvil growTh Analytic (MANTA) model of the anvil shield growth rate. Building on previous works, we model the anvil cloud shield as a single cloud layer fed by detrained cloudy air (Elsaesser et al., 2022; Tiedtke, 1993). The shield extension is estimated by considering an infinitesimally thin cloud layer located at the altitude of the maximum detrainment. The minimal model is simply laid as a source-sink equation, where the source term is the net detrainment and the sink term is approximated by a simple relaxation term, and reads

$$\frac{dA}{dt} = -\frac{1}{\bar{\rho}}\frac{\partial \overline{M}}{\partial z} - \frac{A}{\tau} \quad (1)$$

where A is the anvil cloud shield extension (in m^2) and is obtained by using the TOOCAN cloud tracking algorithm, ρ the density of air in g/m^3, τ the decay coefficient in second, and M is the mass flux $M = \rho A w$ in g/s with w the vertical velocity in m/s.

The $\bar{}$ operator corresponds to horizontal spatial averaging over the anvil cloud shield. $\overline{M}$ is the mass flux average over the whole anvil cloud shield and includes the mass flux originating from convective cells and any non-convective motion :

$$\overline{M} = \overline{M_{convective}} + \overline{M_{non-convective}} \quad (2)$$

The formulation of the source term relies on the net detrainment $\frac{\partial \overline{M}}{\partial z}$, and not the fractional detrainment, as used in other modelling efforts, based on the fact that entrainment is not strong in the upper level of the troposphere especially where the net detrainment is maximum (Elsaesser et al., 2022).

https://doi.org/10.5194/egusphere-2026-6547
Preprint. Discussion started: 30 October 2026
© Author(s) 2026. CC BY 4.0 License.

The sink term follows a simple formulation using a relaxation term proportional to the cloud shield area and a characteristic decay time scale. Various processes (e.g., spreading and thinning, microphysics, sedimentation, mixing, radiative lifting) are encapsulated in the single removal time scale τ (e.g., Lutsko et al. 2026; Seeley et al. 2019; Beydoun et al. 2021). With this formulation of the anvil growth rate, MANTA allows to study the coupling between dynamics (the detrainment considered in the source term) and the microphysics (through the sink term and the parameter τ).

Implementation

The source term

The altitude of the cloud layer is defined as the level of maximum detrainment (LMD), identified using the profile of $-\frac{1}{\bar{\rho}}\frac{\partial \bar{M}}{\partial z}$. The LMD is searched for in each profile within the 9-16km layer to focus on the anvil feeding detrainment and to avoid selecting a warm rain physics induced extremum in the lower part of the troposphere or a feature above the tropopause. Figure 3 shows that, in the simulations, detrainment is positive over a large layer in the upper troposphere corresponding to the anvil cloud top to the anvil base. The profile is characterized by a well marked narrow peak which permits identification of the LMD without ambiguity and enabling consistency with our single layer approximation.

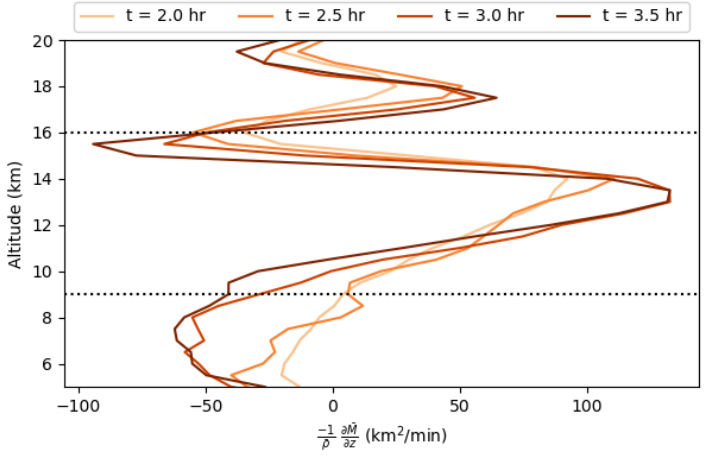

Figure 3: The vertical distribution of detrainment at various steps during the life cycle of a selected system in the SAM simulation (it is the same system as in Figure 4, and we only show the source profile for the time steps of the active phase). The horizontal dotted lines correspond to the lower and upper limits of the layer in which the LMD is searched for.

https://doi.org/10.5194/egusphere-2026-6547
Preprint. Discussion started: 30 October 2026
© Author(s) 2026. CC BY 4.0 License.

Data point selection

The entire growth phase of the system's cloud shield can be decomposed into an initial, an active and a terminating phase (Figure 4a). The first one concerns the first few time steps of the system's life cycle for which usually the growth rate is rather small but still larger than the detrainment source term, preventing the minimal model from working. It is likely that the addition of an extra source term would be required to better describe this initial phase (Elsaesser et al., 2022). The active phase subsequently follows and is characterized by a steady growth (Figure 4b). The terminating phase concerns the time steps following the peak in anvil extension when deep convection vanishes and the shield is about to shrink. While this transition can be more or less abrupt (Roca et al., 2017), it is associated with a change in the cloud shield dynamics (Elsaesser et al., 2022). Trial and error confirmed that the minimal model does not reproduce well the terminating phase of the growth. In the following, we hence restrict our analysis to the growth rates from the active phase. Specifically, the valid points should satisfy: $dA/dt > 0$; $dA/dt <$ Source and $0.1A_{max}<A<0.9A_{max}$. All the points from the active phase of each DCS are pooled together into a single datapool in the following analyses and are termed the valid points.

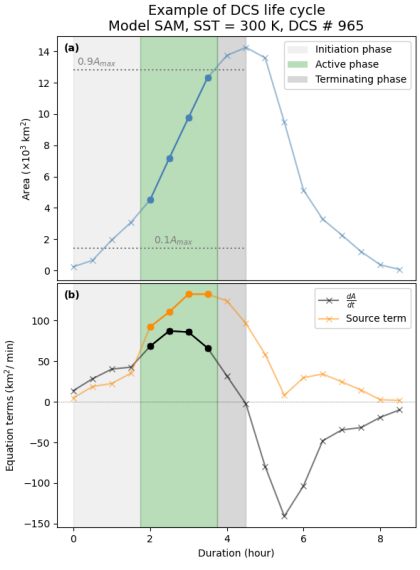

Figure 4: (a) The time evolution of the cloud shield for an individual deep convective system from the SAM simulations; (b) the time evolution of the growth rate and the source term. The light grey, green and grey zone corresponds to the initiation, active and terminating stage of the growth phase.

https://doi.org/10.5194/egusphere-2026-6547
Preprint. Discussion started: 30 October 2026
© Author(s) 2026. CC BY 4.0 License.

With such a definition, the points in the data pool correspond to the valid cloud fraction of the upper level cloudiness of the growth phase. The valid cloud fraction is large, respectively 75, 63, 49% for SAM, MNH and ICON simulations. The strong cut off for ICON is linked to the propension of this model to build small DCSs and by consequence small growth rate values that are more frequently filtered out by the criteria dA/dt < Source than for the other two simulations. These filtered points are more frequent at the earliest part of the system's life cycle. Moreover, thanks to the cloud shield life cycle consistency (Roca et al., 2017), the active phase cloudiness is strongly correlated to the total thick anvil cloudiness of the system (R^2~0.8 in each simulation), making the active phase a very good proxy of thick anvil cloudiness as a whole.

When averaged over all the valid points, the mean LMD corresponds to temperature around 211-219K, depending on the simulations (Figure 5), close to the often quoted 220K level where the water vapor emission starts to dominate the radiative cooling (Hartmann and Larson, 2002).

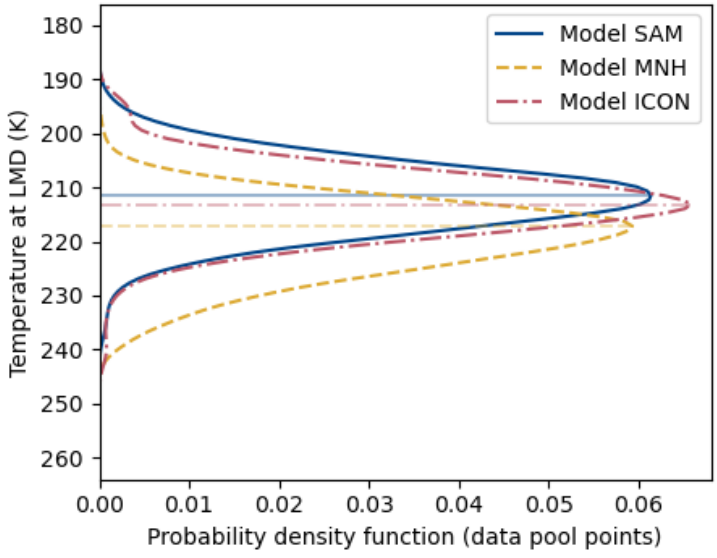

Figure 5: Probability density function of the temperature at the LMD for the three simulations for all the points in the data pool. The horizontal lines mark the maximum of each probability density function.

The sink term

A bulk time decay τ is estimated for each simulation separately by minimizing equation (1). The data are first pooled together by considering, independently, every single value of dA/dt,

https://doi.org/10.5194/egusphere-2026-6547
Preprint. Discussion started: 30 October 2026
© Author(s) 2026. CC BY 4.0 License.

at any moment of the active phase for all of the systems. We use a simple L2 cost function that reads

$$C = \sum_{i=1}^{N} \left[\left(\frac{dA}{dt}\right)_i^{est} - \left(\frac{dA}{dt}\right)_i^{mes} \right]^2 / \sum_{i=1}^{N} \left[\left(\frac{dA}{dt}\right)_i^{mes} \right]^2 \quad (3)$$

where N is the number of points in the data pool. The superscript *est* stands for estimated using equation (1) while *mes* stands for measured directly using the time derivative of the TOOCAN outputs. The data pooling yields 7605, 9044 and 13080 points left for the minimization, for SAM, MNH and ICON respectively.

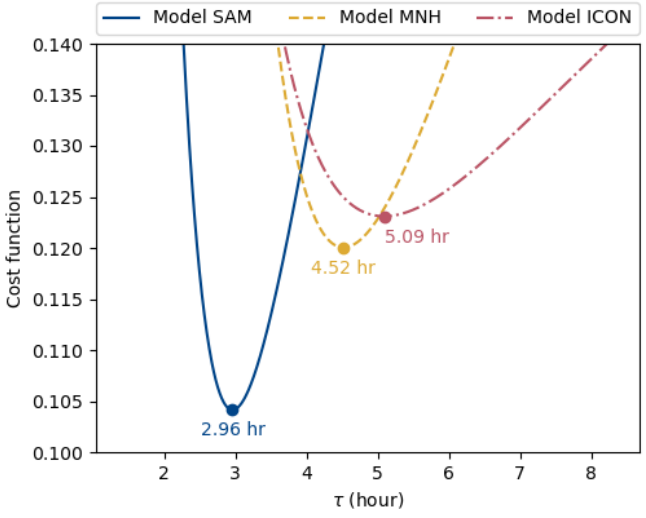

Figure 6 : The cost function and the identified minimum in tau for the three simulations.

Across the simulations, the estimates of τ is ranging from 3 to 5h (Figure 6). This range is rather shorter than the 5-10h estimate of bulk decay time scale from simulations (Seeley et al., 2019). It is slightly larger than reported in a satellite observations study, although in a different framework, and in a drier environmental upper troposphere (Elsaesser et al., 2022). ICON and MNH show a relatively smaller sink term; nevertheless closer to large-scale circulation-derived equivalent (Beydoun et al., 2021). The time decay is influenced by the microphysical scheme used in the simulations (Fan et al., 2017) which likely partly explains the different estimates of the removal characteristic time scale among our three simulations.

The valid points in the data pooling result from the number of systems in the simulations as well as the duration of their growing phases. Longer-lived systems are characterized by a longer growing phase and could hence contribute more to the statistics than shorter systems. Recomputing the decay time parameter with a distribution truncated as a function of the

https://doi.org/10.5194/egusphere-2026-6547
Preprint. Discussion started: 30 October 2026
© Author(s) 2026. CC BY 4.0 License.

duration of the growing phase nevertheless shows a weak sensitivity to the duration (Figure 7). When only 50% of the data pool points coming from the shorter-lived systems are used, the difference between the decay parameter and the original one is 20 min, 40 min, and 9 min for SAM, MNH, and ICON respectively.

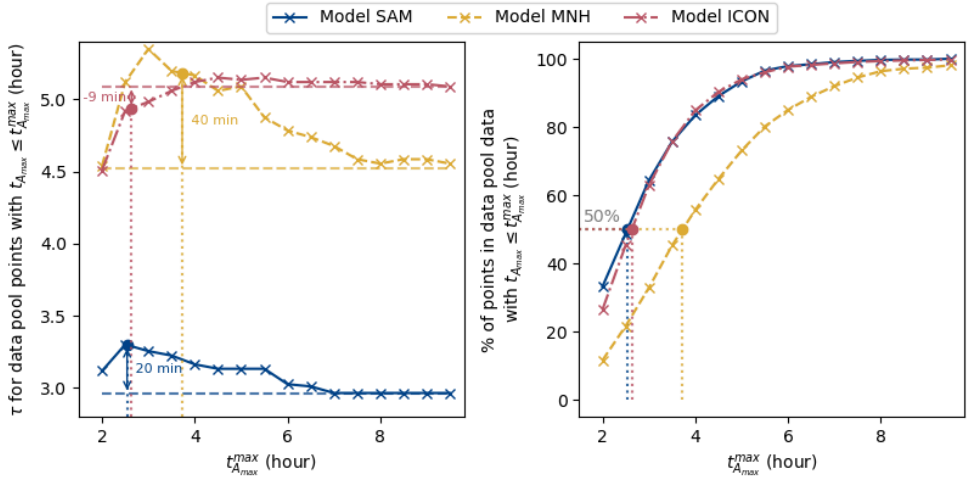

Figure 7: (left) the time decay parameter and (right) the number of points in the data pool, as a function of the growing phase duration for the three simulations. The dotted lines point to the 50% of the data pool coming from the shorter-lived systems. On the left panel, the horizontal dashed lines are the results of the optimization of the decay time on the full data pools.

This results indicates that the contribution to the data pool of less frequent long-lived systems are compensated for by the more frequent short-lived systems (Figure 1) and that the estimation of the decay parameter is not biased towards a given system's duration class.

Performances

The optimized parameter is then used in Equation (1) and the performance of the MANTA model in explaining the simulated growth rates is quantified by comparing the growth rates deduced from Equation (1) to the one directly obtained from TOOCAN (Figure 8). For each of the three simulations, the comparison shows good agreement between the estimated and measured growth rates with correlation coefficient (R^2) in the range 0.64-0.77, a small relative mean absolute error (<30%) and a slope close to one. The robustness of the minimal model performance to the selection of the cloud resolving model further enhances its relevance to describing the underlying physics despite its simplicity.

https://doi.org/10.5194/egusphere-2026-6547
Preprint. Discussion started: 30 October 2026
© Author(s) 2026. CC BY 4.0 License.

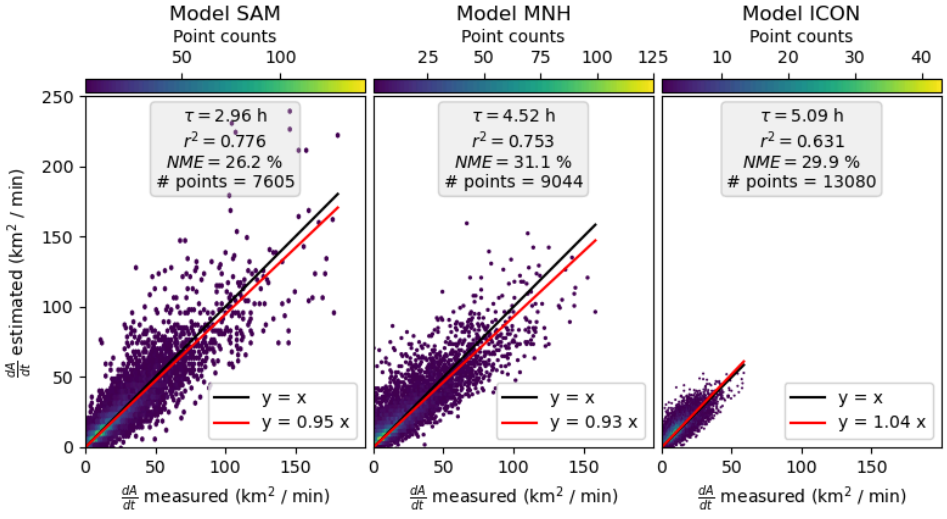

Figure 8: Scatter diagram (for the all data pool) of measured and estimated (with equation (1)) dA/dt for the three simulations. For SAM left, MNH center and ICON right. R^2 is the Pearson correlation coefficient between measured and estimated dA/dt for the data pool. NME stands for Normalized Mean Error (in %), NME=(mean((dA/dt_est - dA/dt))/mean(dA/dt)), each mean value is computed over the datapool. The number of points in each data pool is indicated on the corresponding panel.

The simple model is shown to perform well with TOOCAN derived growth rate, here extracted from numerical simulations which confirm that TOOCAN anvil cloud shield evolutions are physically sound (Elsaesser et al., 2022). These results also support the use of the MANTA model to further analyse the processes contributing to the growth rate.

The importance of the mesoscale dynamics

What is the contribution of the mesoscale to the detrainment?

The contribution of the mesoscale dynamics to the detrainment is evaluated by computing the ratio of the detrainment due only to the columns identified as mesoscale over the anvil cloud shield and the total detrainment (estimated over the whole anvil cloud shield).

The mean relative contribution of the mesoscale to the total detrainment is 45%, 68%, and 87% for SAM, MNH, and ICON respectively. The points for which the mesoscale contributes more than the convective region to the detrainment represent 39%, 75% and 91% of the data pool points in SAM, MNH, and ICON respectively (Figure 9 left). An even larger fraction of the points have a mesoscale contribution above 25%: 79%, 95% and 98%. Thus, the mesoscale part cannot be neglected, and the mean detrainment must be computed over the entire anvil cloud shield rather than over its convective part only. The mesoscale contribution

https://doi.org/10.5194/egusphere-2026-6547
Preprint. Discussion started: 30 October 2026
© Author(s) 2026. CC BY 4.0 License.

is the largest in ICON, where 77% of the data pool points have a mesoscale contribution above 75% of the total detrainment at the LMD.

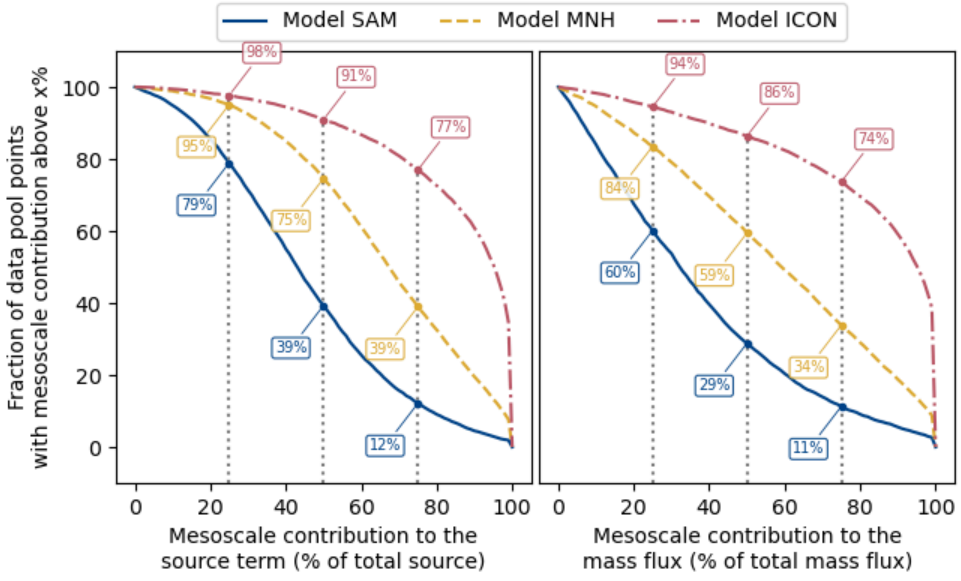

Figure 9: Complementary cumulative distribution of the mesoscale contribution to the detrainment (left) and to the mass flux (right) at the LMD, for SAM, MNH, and ICON. Contributions are expressed as a percentage of the total source term (left) and total mass flux (right). Mass fluxes are evaluated at the LMD. Each curve gives the percentage of data pool points whose mesoscale contribution is above the value on the x-axis.

The same computation is also performed for the mass flux (Figure 9 right). The differences and resemblances between the two distributions (mass flux and detrainment) are similar for each of the three simulations. For the range of mesoscale contributions above ~60%, the two distributions are very similar. At 50% contribution and above, the values are diminished compared to the detrainment distribution and reads 29%, 59% and 86% of the data pool points compared to 39%, 75% and 91% for SAM, MNH, and ICON, respectively. At lower levels of mesoscale contribution the decrease is relatively stronger. The mean contribution of the mesoscale to the mass flux is also diminished for mass flux compared to detrainment and reaches 20%, 60%, and 84% for SAM, MNH, and ICON, respectively. The enhanced mesoscale contribution to the detrainment compared to the mass flux at the LMD arises because of the shape of the vertical mass flux profile. It recalls the fundamental difference between the mass flux and the detrainment and its importance to the anvil growth physics.

https://doi.org/10.5194/egusphere-2026-6547
Preprint. Discussion started: 30 October 2026
© Author(s) 2026. CC BY 4.0 License.

Do we need the mesoscale?

The importance of the mesoscale dynamics is further assessed by comparing alternative implementations of the MANTA model with the original. Mechanism-denial experiments are performed to build three alternatives to the original implementation of MANTA. The first experiment consists in restricting the computation of the detrainment to the convective part of the DCS, i.e. setting $\overline{M} = \overline{M_{convective}}$. The LMD is recomputed for these new detrainment profiles in order to obtain the source term of the equation and does not change much from the original experiment (not shown). The selection of points follows the same logic as described above. Because the source term now differs, the condition dA/dt > Source selects a new subset of data points for which MANTA is valid. The optimization is performed again on this new data pool to obtain τ. In the following, this version of MANTA, restricted to the convective detrainment, is identified as CONVONLY. In the second experiment, the sink term is removed ($\tau = \infty$) and the source is kept as in the original (experiment NOSINK). Finally, in the third experiment, we use the source term computed from the convective detrainment and remove the sink term (experiment CONVONLY_NOSINK).

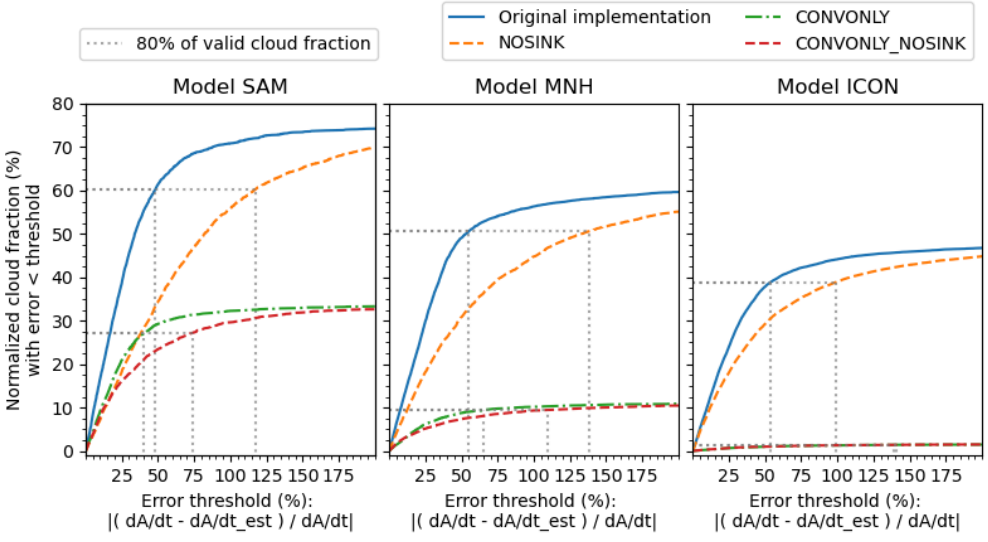

Figure 10: Cumulated distributions of the absolute magnitude of relative errors for various configurations of the model for the simulations for SAM (left), MNH (middle) and ICON (right).The gray lines point to the 80% population level.

https://doi.org/10.5194/egusphere-2026-6547
Preprint. Discussion started: 30 October 2026
© Author(s) 2026. CC BY 4.0 License.

300K	Original implementation				CONVONLY				NOSINK				CONVONLY_NOSINK			
	R^2	NME	slope	Valid cloud fraction	R^2	NME	slope	valid cloud fraction	R^2	NME	slope	Valid cloud fraction	R^2	NME	slope	Valid cloud fraction
SAM	0.78	26 %	0.95	75.4 %	0.84	21%	1.0	33.9 %	0.79	53%	1.5	75.4 %	0.87	32%	1.3	33.9 %
MNH	0.75	31%	0.93	63.3 %	0.79	27%	0.99	11.8 %	0.76	56%	1.41	63.3 %	0.81	38%	1.2	11.8 %
ICON	0.63	30%	1.04	48.6 %	0.69	36%	1.13	1.8 %	0.72	43%	1.31	48.6 %	0.73	44%	1.3	1.8 %

Table 2: Pearson linear correlation coefficient (R^2) , normalized mean error (NME) defined as NME=(mean((dA/dt_est - dA/dt))/mean(dA/dt)) and slope of the regression between estimated and TOOCAN growth rates. The valid cloud fraction is defined as the cumulated area of the active phase normalized by the cumulated area of the growth phase between 0.1Amax and 0.9Amax.

In addition to the previously used performance metrics (R^2 and NME), we also compute the valid cloud fraction for each of the experiments. It is defined as the fraction of the cloudiness associated with all the growing phases of all the systems that corresponds to the data pool (see Section Data point selection). Because the CONVONLY experiments alter the source, the test dA/dt < Source in the data selection procedure impacts the number of points that are valid.

The results of the analysis are shown in Table 2 and summarized in Figure 10. The results are robust over the three simulations. For the CONVONLY, NOSINK and CONVONLY_NOSINK experiments, correlation coefficient (R^2) between estimated and measured growth rate are similar to the original model performances. The normalized mean error (NME) is also very similar between the alternative implementation (NOSINK excepted) and the original one.

When applied to SAM and MNH, the CONVONLY experiment yields larger values of τ than the original implementation, respectively 6.5 and 12.9 hours. This is consistent with the suppression of the mesoscale contribution to the detrainment which decreases the source term, that is balanced by a smaller sink (larger tau), everything else being equal. For ICON, although a large fraction of the detrainment is due to mesoscale (Figure 9), altering the source, has limited impact to the estimation of tau which now reads 4.8h compared to the original 5.1h. This is linked to a compensating effect of the anvil area of the valid points which only encompasses ~2% of the original cases in this experiment compared to the original one. This simple link between source and tau revealed by the minimal model could explain the difference between the removal time scale reported here and in the literature, by pointing to a missing detrainment source.

Beyond correlation and normalized mean error, the valid cloud fraction of CONVONLY experiment strongly changes when compared to the original implementation. As the condition

https://doi.org/10.5194/egusphere-2026-6547
Preprint. Discussion started: 30 October 2026
© Author(s) 2026. CC BY 4.0 License.

dA/dt < Source, under which MANTA is valid, is less readily satisfied when the source term is computed only over the convective part of the DCS, the active phase of each DCS is diminished, leading to a smaller data pool. For SAM, the cloud fraction of the data pool shrinks by a factor ~2, for MNH, it falls by a factor ~6, while for ICON, the remaining points in the data pool only contribute to ~2% of the global cloud fraction. Thus, a simple source-sink model for which the source is restricted to the convective detrainment would be relevant to describe only a very limited fraction of the thick anvil cloudiness, much less that the same model would yield by incorporating the contribution of mesoscale dynamics to the source term.

The NOSINK experiment for which the sink is removed exhibits significantly degraded statistical performances for all three simulations. It is characterized by an increase in the NME and an increase in the regression slope expressing the strong overestimation of the growth rate in such a configuration and revealing the importance of the missing sink. The NME of the CONVONLY_NOSINK experiment is in between the NOCONV and NOSINK values. The CONVONLY_NOSINK experiment has degraded slopes and the same limited applicability than in the CONVONLY case.

Discussion

The results of this study highlight that the expression of the coupling between dynamics and microphysics cannot be limited to convection only to properly describe the anvil growth rate. The source term should include dynamical contributions that we term “mesoscale dynamics” which refers to the non-convective motions inside the anvil. These motions initiate from older, weaker convection, forming an intermediate region between new deep convection and the stratiform region. It also encompasses the stratiform upper level lifting area and significantly contributes to the net upward mass flux (Houze, 1997). The significant contribution of non-convective motions to the net detrainment arises from their large spatial extension within the cloud shield. Despite weaker velocities than their convective counterparts, these buoyant air masses have a significant contribution to the detrainment when encountering the upper level stable layer. It is consistent with early numerical experiments showing that the suppression of mesoscale updrafts leads to the production of an incipient cirrus layer (*cirrostratus cumulonimbogenitus*) and not an anvil (Churchill and Houze, 1991).

The MANTA model establishes that the instantaneous growth rate results from a balance between the source, including both convective and mesoscale contributions, and the sink. This balance is detailed in Figure 11. For a given growth rate, SAM needs a stronger sink compared to the other models as its source term is also relatively larger. On average over the whole data pool, the source (resp. sink) term represents 166% (resp. 66%) of the growth rate. MNH exhibits a scenario close to that of SAM, with a mean source (resp. sink) to growth rate ratio of 155% (resp. 55%). Conversely, ICON produces less, and removes less ice to reach the same growth rate: on average, the source (resp. sink) term represents only 138% (resp. 38%) of the growth rate. These relative contributions remain roughly constant across the

https://doi.org/10.5194/egusphere-2026-6547
Preprint. Discussion started: 30 October 2026
© Author(s) 2026. CC BY 4.0 License.

whole range of growth rates in the data pool for each model, as shown in Figure 11. For all three models, a weaker source is consistent with a longer removal time scale: τ increase from SAM to MNH to ICON. However, the way the sink balances the source is also influenced by the underlying area distributions.

The relative changes of the mean sink $\overline{S}$ when comparing one simulation to another can indeed be written as as function of $\overline{A}$ and τ

$$\frac{\Delta\overline{S}}{\overline{S}} = \frac{\Delta\overline{A}}{\overline{A}} - \frac{\Delta\tau}{\tau} \quad (4)$$

where the Δ stands for the difference between two simulations and are summarized in Table 3. The strong decrease of the sink between SAM and ICON results from the addition of a decrease in the mean anvil cloud shield area (due to an underlying area distribution in ICON that is narrower, with a less extended tail of large anvils, and more numerous small anvil clouds) and an increase of the time decay parameter. Similarly for the difference between MNH and ICON, the decrease in the sink results from the addition of both terms of Eq. (4). On the other hand, the comparison between SAM and MNH shows that the small decrease in the mean sink results from a balance between the increase in both the mean anvil area (the two underlying area distributions scale to each other) and the decay parameter among the two simulations. Hence, the resemblance between SAM and MNH and the difference with ICON concerning the role of the sink (A/τ) for a given growth rate cannot be explained solely with the difference in the time decay parameter that incorporates the cloud microphysics. The coupling between dynamics, diabatic heating and cloudiness (e.g., Tao et al. 2022) eventually also needs to be invoked to yield to the estimated balance.

	$\Delta\overline{S}/\overline{S}$	$\Delta\overline{A}/\overline{A}$	$-\ \Delta\tau/\tau$
ICON-SAM	-133%	-79%	-54%
SAM-MNH	-25%	+17%	-42%
ICON-MNH	-108%	-96%	-12%

Table 3: Relative changes of the mean sink from one simulation to another.

https://doi.org/10.5194/egusphere-2026-6547
Preprint. Discussion started: 30 October 2026
© Author(s) 2026. CC BY 4.0 License.

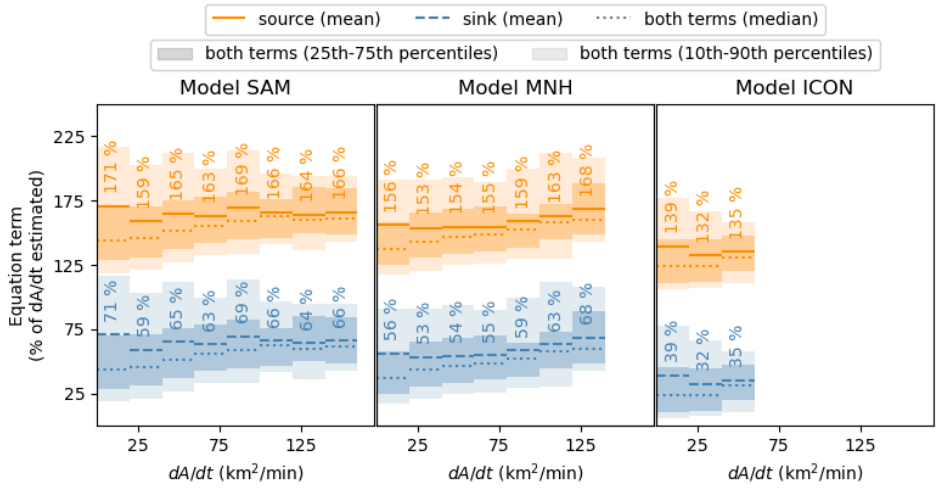

Figure 11: Evolution of the contribution of the source and the sink as a function of the growth rate. Plain and dashed lines (resp. dotted) are the mean (resp. median). The darker (resp. lighter) shading corresponds to the 25-75th (resp. 10-90th) percentiles. Bins of dA/dt have a width of 20km2/min, bins populated with less than 10 points were excluded. The written values correspond to the mean in each bin.

Conclusion and outlook

RCE simulations at km scale are used together with a cloud tracking algorithm to analyse the growth rate of the anvil cloud shield. Despite the highly idealized numerical setup, the simulated growth rates are shown to reproduce the variability over the growing phase, a key feature of the satellite observed deep convective systems cloud shield. The 25 days of simulations from three different cloud resolving models with different dynamical cores, turbulence closures and microphysical assumptions provide a large diversity of simulated growth rates allowing a detailed investigation of the processes at play during the growing phase of the deep convective systems.

The Minimal ANvil growTh Analytic (MANTA) model of the anvil shield is introduced to help analyze the simulations in a physically transparent way. The functional form of this simple model is a simplification of the Elsaesser et al. (2022) work and resumes the growth rate as the balance between a detrainment source estimated at the level of maximum detrainment and a simple sink. The sink is characterized by a decay parameter, the single parameter of the model. The MANTA model is shown to fit well the numerical simulations from the three cloud resolving models. Mechanisms denial experiments further indicate that truncated implementations of the MANTA model are not performing as well as the currently original one. In this sense, MANTA is indeed a minimal model and no simpler formulation

https://doi.org/10.5194/egusphere-2026-6547
Preprint. Discussion started: 30 October 2026
© Author(s) 2026. CC BY 4.0 License.

(nor implementation) performs as well. The usefulness of this class of simple source-sink model, originally implemented in a satellite observations perspective (Elsaesser et al., 2022), is shown to extend to km-scale simulations. It confirms the fitness between the TOOCAN derived growth rate of anvil cloud shield and this class of model.

The study shows that across the three simulations, the time decay parameter of the MANTA model varies from 3 to 5h which is related to the need for a more or less effective sink to produce a given growth rate. SAM needs a stronger sink compared to the other models as its source term is also relatively larger. MNH exhibits a scenario close to that of SAM. Conversely, ICON produces less, and removes less ice to reach the same growth rate. The fact that the sampling of the growing phase could be influenced by the longer-lived ones is ruled out thanks to a sensitivity analysis that indicates a weak dependence of the estimation to the duration of the growing phase. All the three models do indicate that this partitioning is near constant across the whole range of growth rates.

The source term is decomposed using a convective/mesoscale mask and the quantitative analysis reveals the importance of the mesoscale dynamics, in complement to the convective motions, to the detrainment that builds the anvil. It is shown that the contribution of the mesoscale is significant compared to that of convection and cannot be neglected in the anvil cloud shield budget. The behavior of the detrainment vs. the mass flux is clarified. It is shown that the mesoscale contribution to the detrainment is enhanced compared to that of the mass flux at the LMD.

While previous investigations focused on the sink term, promoting for instance, sublimation (or lack thereof) (Seeley et al., 2019) or sedimentation (Beydoun et al., 2021) as important controlling factors of the time decay parameter, we here explored the source term. It would nevertheless be of interest to assess the various microphysical pathways to the estimation of the time decay parameter in the present framework. Numerical sensitivity experiments by modifying the microphysical scheme are left out for future work.

Whether the invariance of the partitioning between the source and sink with the growth rate is a RCE feature or a more fundamental characteristic of tropical convection deserves more investigation. Realistic configurations of emerging km scale climate models are showing encouraging results as far as the simulation of the life cycle deep convective systems' cloud shield is concerned (Abramian et al., 2025; Feng et al., 2025; Prein et al., 2024). Applying our diagnostic approach to such realistic simulations could clarify this question.

Finally, the success of the MANTA model combined with TOOCAN is a strong impetus to build on this minimal formulation. Efforts towards characterizing more anvil properties like the ice water path time evolution and the radiative properties of the anvil cloud shield, in complement to the area growth rate, keeping the present low order modelling perspective (e.g., Deutloff et al. 2025), will be undertaken in the future.

https://doi.org/10.5194/egusphere-2026-6547
Preprint. Discussion started: 30 October 2026
© Author(s) 2026. CC BY 4.0 License.

Data availability

We will make the data available by the publication time.

Code availability

The TOOCAN algorithm is open source and is available. We will make the data link by the publication time. The data analysis codes are available upon request to the authors.

Author Contributions

RR designed the study in discussion with TF, CH and GSE. TF performed the tracking on the simulations. LA led the data analysis and the visualisation. NA contributed to the data analysis. RR computed the OLR-BT relationships. CM, JPC and RF performed the cloud resolving simulations for SAM, MNH and ICON respectively. All authors discussed the results and contributed to the manuscript preparation.

Competing Interests

The authors declare that they have no conflict of interest.

Disclaimer

Copernicus Publications remains neutral with regard to jurisdictional claims made in the text, published maps, institutional affiliations, or any other geographical representation in this paper. While Copernicus Publications makes every effort to include appropriate place names, the final responsibility lies with the authors. Views expressed in the text are those of the authors and do not necessarily reflect the views of the publisher.

Acknowledgments

We thank S. Cloché for her support with the handling of these various datasets. This study benefited from the IPSL mesocenter ESPRI facility which is supported by CNRS, UPMC, Labex L-IPSL, CNES and Ecole Polytechnique. Artificial Intelligence has been used to correct English spelling, grammar and sentence structure.

Financial Support

https://doi.org/10.5194/egusphere-2026-6547
Preprint. Discussion started: 30 October 2026
© Author(s) 2026. CC BY 4.0 License.

The authors acknowledge the financial support of CNES, France (ROR: https://ror.org/04h1h0y33), within the framework of the C2OMODO mission. Computer resources for running Meso-NH were allocated by GENCI (grant A0200111437). JPC acknowledges the French National Research Infrastructure CLIMERI-France (https://climeri-france.fr/) which provides a national label for the code Meso-NH. GSE acknowledges support from the APAM-GISS Cooperative Agreement 80NSSC18M0133, a NASA Precipitation Measurement Missions Grant 80NSSC22K0609, and the NASA PolSIR Mission (80LARC24CA001).

References

Abramian, S., Muller, C., Risi, C., Fiolleau, T., and Roca, R.: How key features of early development shape deep convective systems, Npj Clim. Atmos. Sci., 8, 258, https://doi.org/10.1038/s41612-025-01154-1, 2025.

Ackerman, T. P., Liou, K.-N., Valero, F. P. J., and Pfister, L.: Heating Rates in Tropical Anvils, J. Atmos. Sci., 45, 1606–1623, https://doi.org/10.1175/1520-0469(1988)045%3C1606:HRITA%3E2.0.CO;2, 1988.

Baldauf, M., Seifert, A., Förstner, J., Majewski, D., Raschendorfer, M., and Reinhardt, T.: Operational Convective-Scale Numerical Weather Prediction with the COSMO Model: Description and Sensitivities, Mon. Weather Rev., 139, 3887–3905, https://doi.org/10.1175/MWR-D-10-05013.1, 2011.

Beydoun, H., Caldwell, P. M., Hannah, W. M., and Donahue, A. S.: Dissecting Anvil Cloud Response to Sea Surface Warming, Geophys. Res. Lett., 48, e2021GL094049, https://doi.org/10.1029/2021GL094049, 2021.

Bougeault, P. and Lacarrere, P.: Parameterization of Orography-Induced Turbulence in a Mesobeta--Scale Model, Mon. Weather Rev., 117, 1872–1890, https://doi.org/10.1175/1520-0493(1989)117%3C1872:POOITI%3E2.0.CO;2, 1989.

Bouniol, D., Roca, R., Fiolleau, T., and Poan, D. E.: Macrophysical, Microphysical, and Radiative Properties of Tropical Mesoscale Convective Systems over Their Life Cycle, J. Clim., 29, 3353–3371, https://doi.org/10.1175/JCLI-D-15-0551.1, 2016.

Churchill, D. D. and Houze, R. A.: Effects of Radiation and Turbulence on the Diabatic Heating and Water Budget of the Stratiform Region of a Tropical Cloud Cluster, J. Atmos. Sci., 48, 903–922, https://doi.org/10.1175/1520-0469(1991)048%3C0903:EORATO%3E2.0.CO;2, 1991.

Cuxart, J., Bougeault, P., and Redelsperger, J. -L.: A turbulence scheme allowing for mesoscale and large-eddy simulations, Q. J. R. Meteorol. Soc., 126, 1–30, https://doi.org/10.1002/qj.49712656202, 2000.

Deutloff, J., Buehler, S. A., Brath, M., and Naumann, A. K.: Insights on Tropical High-Cloud Radiative Effect From a New Conceptual Model, J. Adv. Model. Earth Syst., 17, e2024MS004615, https://doi.org/10.1029/2024MS004615, 2025.

https://doi.org/10.5194/egusphere-2026-6547
Preprint. Discussion started: 30 October 2026
© Author(s) 2026. CC BY 4.0 License.

Elsaesser, G. S., Roca, R., Fiolleau, T., Del Genio, A. D., and Wu, J.: A Simple Model for Tropical Convective Cloud Shield Area Growth and Decay Rates Informed by Geostationary IR, GPM, and Aqua/AIRS Satellite Data, J. Geophys. Res. Atmos., 127, e2021JD035599, https://doi.org/10.1029/2021JD035599, 2022.

Fan, J., Han, B., Varble, A., Morrison, H., North, K., Kollias, P., Chen, B., Dong, X., Giangrande, S. E., Khain, A., Lin, Y., Mansell, E., Milbrandt, J. A., Stenz, R., Thompson, G., and Wang, Y.: Cloud-resolving model intercomparison of an MC3E squall line case: Part I—Convective updrafts, J. Geophys. Res. Atmos., 122, 9351–9378, https://doi.org/10.1002/2017JD026622, 2017.

Feng, Z., Prein, A. F., Kukulies, J., Fiolleau, T., Jones, W. K., Maybee, B., Moon, Z. L., Núñez Ocasio, K. M., Dong, W., Molina, M. J., Albright, M. G., Rajagopal, M., Robledo, V., Song, J., Song, F., Leung, L. R., Varble, A. C., Klein, C., Roca, R., Feng, R., and Mejia, J. F.: Mesoscale Convective Systems Tracking Method Intercomparison (MCSMIP): Application to DYAMOND Global km-Scale Simulations, J. Geophys. Res. Atmos., 130, e2024JD042204, https://doi.org/10.1029/2024JD042204, 2025.

Fiolleau, T. and Roca, R.: An Algorithm for the Detection and Tracking of Tropical Mesoscale Convective Systems Using Infrared Images From Geostationary Satellite, IEEE Trans. Geosci. Remote Sens., 51, 4302–4315, https://doi.org/10.1109/TGRS.2012.2227762, 2013.

Fiolleau, T. and Roca, R.: A database of deep convective systems derived from the intercalibrated meteorological geostationary satellite fleet and the TOOCAN algorithm (2012–2020), Earth Syst. Sci. Data, 16, 4021–4050, https://doi.org/10.5194/essd-16-4021-2024, 2024.

Fiolleau, T., Roca, R., Cloche, S., Bouniol, D., and Raberanto, P.: Homogenization of Geostationary Infrared Imager Channels for Cold Cloud Studies Using Megha-Tropiques/ScaRaB, IEEE Trans. Geosci. Remote Sens., 58, 6609–6622, https://doi.org/10.1109/TGRS.2020.2978171, 2020.

Fouquart, Y. and Bonnel, B.: Computations of Solar Heating of the Earth's Atmosphere—A New Parameterization, , Beitrage Zur Phys. Atmos.5335–62, 1980.

Gasparini, B., Blossey, P. N., Hartmann, D. L., Lin, G., and Fan, J.: What Drives the Life Cycle of Tropical Anvil Clouds?, J. Adv. Model. Earth Syst., 11, 2586–2605, https://doi.org/10.1029/2019MS001736, 2019.

Gasparini, B., Sullivan, S. C., Sokol, A. B., Kärcher, B., Jensen, E., and Hartmann, D. L.: Opinion: Tropical cirrus – from micro-scale processes to climate-scale impacts, Atmos. Chem. Phys., 23, 15413–15444, https://doi.org/10.5194/acp-23-15413-2023, 2023a.

Gasparini, B., Sullivan, S. C., Sokol, A. B., Kärcher, B., Jensen, E., and Hartmann, D. L.: Opinion: Tropical cirrus – from micro-scale processes to climate-scale impacts, Atmos. Chem. Phys., 23, 15413–15444, https://doi.org/10.5194/acp-23-15413-2023, 2023b.

Gasparini, B., Atlas, R., Voigt, A., Krämer, M., and Blossey, P. N.: Tropical cirrus evolution in a kilometer-scale model with improved ice microphysics, Atmos. Chem. Phys., 25, 9957–9979, https://doi.org/10.5194/acp-25-9957-2025, 2025.

https://doi.org/10.5194/egusphere-2026-6547
Preprint. Discussion started: 30 October 2026
© Author(s) 2026. CC BY 4.0 License.

Geer, A. J., Bauer, P., Lonitz, K., Barlakas, V., Eriksson, P., Mendrok, J., Doherty, A., Hocking, J., and Chambon, P.: Bulk hydrometeor optical properties for microwave and sub-millimetre radiative transfer in RTTOV-SCATT v13.0, Geosci. Model Dev., 14, 7497–7526, https://doi.org/10.5194/gmd-14-7497-2021, 2021.

Hartmann, D. L. and Berry, S. E.: The balanced radiative effect of tropical anvil clouds, J. Geophys. Res. Atmos., 122, 5003–5020, https://doi.org/10.1002/2017JD026460, 2017.

Hartmann, D. L. and Larson, K.: An important constraint on tropical cloud - climate feedback, Geophys. Res. Lett., 29, https://doi.org/10.1029/2002GL015835, 2002.

Hartmann, D. L., Gasparini, B., Berry, S. E., and Blossey, P. N.: The Life Cycle and Net Radiative Effect of Tropical Anvil Clouds, J. Adv. Model. Earth Syst., 10, 3012–3029, https://doi.org/10.1029/2018MS001484, 2018.

Hohenegger, C., Korn, P., Linardakis, L., Redler, R., Schnur, R., Adamidis, P., Bao, J., Bastin, S., Behravesh, M., Bergemann, M., Biercamp, J., Bockelmann, H., Brokopf, R., Brüggemann, N., Casaroli, L., Chegini, F., Datseris, G., Esch, M., George, G., Giorgetta, M., Gutjahr, O., Haak, H., Hanke, M., Ilyina, T., Jahns, T., Jungclaus, J., Kern, M., Klocke, D., Kluft, L., Kölling, T., Kornblueh, L., Kosukhin, S., Kroll, C., Lee, J., Mauritsen, T., Mehlmann, C., Mieslinger, T., Naumann, A. K., Paccini, L., Peinado, A., Praturi, D. S., Putrasahan, D., Rast, S., Riddick, T., Roeber, N., Schmidt, H., Schulzweida, U., Schütte, F., Segura, H., Shevchenko, R., Singh, V., Specht, M., Stephan, C. C., Von Storch, J.-S., Vogel, R., Wengel, C., Winkler, M., Ziemen, F., Marotzke, J., and Stevens, B.: ICON-Sapphire: simulating the components of the Earth system and their interactions at kilometer and subkilometer scales, Geosci. Model Dev., 16, 779–811, https://doi.org/10.5194/gmd-16-779-2023, 2023.

Houze, Jr., R. A.: Cloud Clusters and Large-Scale Vertical Motions in the Tropics, J. Meteorol. Soc. Jpn. Ser II, 60, 396–410, https://doi.org/10.2151/jmsj1965.60.1_396, 1982.

Houze, R. A.: Cloud dynamics, Academic Press, San Diego, 573 pp., 1993.

Houze, R. A.: Stratiform Precipitation in Regions of Convection: A Meteorological Paradox?, Bull. Am. Meteorol. Soc., 78, 2179–2196, https://doi.org/10.1175/1520-0477(1997)078%3C2179:SPIROC%3E2.0.CO;2, 1997.

Houze, R. A.: Mesoscale convective systems, Rev. Geophys., 42, 2004RG000150, https://doi.org/10.1029/2004RG000150, 2004.

Khairoutdinov, M. F. and Randall, D. A.: Cloud Resolving Modeling of the ARM Summer 1997 IOP: Model Formulation, Results, Uncertainties, and Sensitivities, J. Atmos. Sci., 60, 607–625, https://doi.org/10.1175/1520-0469(2003)060%3C0607:CRMOTA%3E2.0.CO;2, 2003.

Lac, C., Chaboureau, J.-P., Masson, V., Pinty, J.-P., Tulet, P., Escobar, J., Leriche, M., Barthe, C., Aouizerats, B., Augros, C., Aumond, P., Auguste, F., Bechtold, P., Berthet, S., Bielli, S., Bosseur, F., Caumont, O., Cohard, J.-M., Colin, J., Couvreux, F., Cuxart, J., Delautier, G., Dauhut, T., Ducrocq, V., Filippi, J.-B., Gazen, D., Geoffroy, O., Gheusi, F., Honnert, R., Lafore, J.-P., Lebeaupin Brossier, C., Libois, Q., Lunet, T., Mari, C., Maric, T., Mascart, P., Mogé, M., Molinié, G., Nuissier, O., Pantillon, F., Peyrillé, P., Pergaud, J., Perraud, E.,

https://doi.org/10.5194/egusphere-2026-6547
Preprint. Discussion started: 30 October 2026
© Author(s) 2026. CC BY 4.0 License.

Pianezze, J., Redelsperger, J.-L., Ricard, D., Richard, E., Riette, S., Rodier, Q., Schoetter, R., Seyfried, L., Stein, J., Suhre, K., Taufour, M., Thouron, O., Turner, S., Verrelle, A., Vié, B., Visentin, F., Vionnet, V., and Wautelet, P.: Overview of the Meso-NH model version 5.4 and its applications, Geosci. Model Dev., 11, 1929–1969, https://doi.org/10.5194/gmd-11-1929-2018, 2018.

Lilly, D. K.: On the numerical simulation of buoyant convection, Tellus, 14, 148–172, https://doi.org/10.1111/j.2153-3490.1962.tb00128.x, 1962.

Lilly, D. K.: Cirrus Outflow Dynamics, J. Atmos. Sci., 45, 1594–1605, https://doi.org/10.1175/1520-0469(1988)045%3C1594:COD%3E2.0.CO;2, 1988.

Lutsko, N. J., Wall, C. J., and Gasparini, B.: An Analytical Model of the Lifecycle of Tropical Anvil Cloud Radiative Effects, J. Geophys. Res. Atmos., 131, e2025JD045070, https://doi.org/10.1029/2025JD045070, 2026.

Maddox, R. A.: Meoscale Convective Complexes, Bull. Am. Meteorol. Soc., 61, 1374–1387, https://doi.org/10.1175/1520-0477(1980)061%3C1374:MCC%3E2.0.CO;2, 1980.

Maher, P., Gerber, E. P., Medeiros, B., Merlis, T. M., Sherwood, S., Sheshadri, A., Sobel, A. H., Vallis, G. K., Voigt, A., and Zurita-Gotor, P.: Model Hierarchies for Understanding Atmospheric Circulation, Rev. Geophys., 57, 250–280, https://doi.org/10.1029/2018RG000607, 2019.

Marinescu, P. J., Van Den Heever, S. C., Saleeby, S. M., and Kreidenweis, S. M.: The microphysical contributions to and evolution of latent heating profiles in two MC3E MCSs, J. Geophys. Res. Atmos., 121, 7913–7935, https://doi.org/10.1002/2016JD024762, 2016.

Mlawer, E. J., Taubman, S. J., Brown, P. D., Iacono, M. J., and Clough, S. A.: Radiative transfer for inhomogeneous atmospheres: RRTM, a validated correlated-k model for the longwave, J. Geophys. Res. Atmos., 102, 16663–16682, https://doi.org/10.1029/97JD00237, 1997.

Mu, Q., Ge, J., Huang, J., Hu, X., Peng, N., Li, Y., Wang, M., Zhang, J., Xu, Z., Zhang, C., and Liu, B.: A New Classification of In Situ and Anvil Cirrus Clouds Uncovers Their Properties and Interhemispheric Connections, AGU Adv., 6, e2025AV001919, https://doi.org/10.1029/2025AV001919, 2025.

Netz, L., Fiolleau, T., and Roca, R.: A method for characterizing the spatial organization of deep convective cores in deep convective systems' cloud shield using idealized elementary convective structure decomposition, Atmos. Meas. Tech., 18, 7603–7628, https://doi.org/10.5194/amt-18-7603-2025, 2025.

Pergaud, J., Masson, V., Malardel, S., and Couvreux, F.: A Parameterization of Dry Thermals and Shallow Cumuli for Mesoscale Numerical Weather Prediction, Bound.-Layer Meteorol., 132, 83–106, https://doi.org/10.1007/s10546-009-9388-0, 2009.

Pincus, R., Mlawer, E. J., and Delamere, J. S.: Balancing Accuracy, Efficiency, and Flexibility in Radiation Calculations for Dynamical Models, J. Adv. Model. Earth Syst., 11, 3074–3089, https://doi.org/10.1029/2019MS001621, 2019.

https://doi.org/10.5194/egusphere-2026-6547
Preprint. Discussion started: 30 October 2026
© Author(s) 2026. CC BY 4.0 License.

Pinty, J.-P. and P. Jabouille: A mixed-phase cloud parameterization for use in a mesoscale non-hydrostatic model: Simulations of a squall line and of orographic precipitation, in: Proc. Conf. on Cloud Physics, Proc. Conf. on Cloud Physics, 217–220, 1998.

Prein, A. F., Feng, Z., Fiolleau, T., Moon, Z. L., Núñez Ocasio, K. M., Kukulies, J., Roca, R., Varble, A. C., Rehbein, A., Liu, C., Ikeda, K., Mu, Y., and Rasmussen, R. M.: Km-Scale Simulations of Mesoscale Convective Systems Over South America—A Feature Tracker Intercomparison, J. Geophys. Res. Atmos., 129, e2023JD040254, https://doi.org/10.1029/2023JD040254, 2024.

Roca, R. and Ramanathan, V.: Scale Dependence of Monsoonal Convective Systems over the Indian Ocean, J. Clim., 13, 1286–1298, https://doi.org/10.1175/1520-0442(2000)013%3C1286:SDOMCS%3E2.0.CO;2, 2000.

Roca, R., Fiolleau, T., and Bouniol, D.: A Simple Model of the Life Cycle of Mesoscale Convective Systems Cloud Shield in the Tropics, J. Clim., 30, 4283–4298, https://doi.org/10.1175/JCLI-D-16-0556.1, 2017.

Saunders, R., Hocking, J., Turner, E., Rayer, P., Rundle, D., Brunel, P., Vidot, J., Roquet, P., Matricardi, M., Geer, A., Bormann, N., and Lupu, C.: An update on the RTTOV fast radiative transfer model (currently at version 12), Geosci. Model Dev., 11, 2717–2737, https://doi.org/10.5194/gmd-11-2717-2018, 2018.

Seeley, J. T., Jeevanjee, N., Langhans, W., and Romps, D. M.: Formation of Tropical Anvil Clouds by Slow Evaporation, Geophys. Res. Lett., 46, 492–501, https://doi.org/10.1029/2018GL080747, 2019.

Smagorinsky, J.: General circulation experiments with the primitive equations: 1. The basic experiment, Mon. Weather Rev., 91, 99–164, https://doi.org/10.1175/1520-0493(1963)091%3C0099:GCEWTP%3E2.3.CO;2, 1963.

Stephens, G. L., Vane, D. G., Tanelli, S., Im, E., Durden, S., Rokey, M., Reinke, D., Partain, P., Mace, G. G., Austin, R., L'Ecuyer, T., Haynes, J., Lebsock, M., Suzuki, K., Waliser, D., Wu, D., Kay, J., Gettelman, A., Wang, Z., and Marchand, R.: CloudSat mission: Performance and early science after the first year of operation, J. Geophys. Res. Atmos., 113, 2008JD009982, https://doi.org/10.1029/2008JD009982, 2008.

Stephens, G. L., Shiro, K. A., Hakuba, M. Z., Takahashi, H., Pilewskie, J. A., Andrews, T., Stubenrauch, C. J., and Wu, L.: Tropical Deep Convection, Cloud Feedbacks and Climate Sensitivity, Surv. Geophys., 45, 1903–1931, https://doi.org/10.1007/s10712-024-09831-1, 2024.

Takahashi, H., Luo, Z. J., and Stephens, G. L.: Level of neutral buoyancy, deep convective outflow, and convective core: New perspectives based on 5 years of CloudSat data, J. Geophys. Res. Atmos., 122, 2958–2969, https://doi.org/10.1002/2016JD025969, 2017.

Takasuka, D., Kodama, C., Suematsu, T., Ohno, T., Yamada, Y., Seiki, T., Yashiro, H., Nakano, M., Miura, H., Noda, A. T., Nasuno, T., Miyakawa, T., and Masunaga, R.: How Can We Improve the Seamless Representation of Climatological Statistics and Weather Toward Reliable Global K-Scale Climate Simulations?, J. Adv. Model. Earth Syst., 16, e2023MS003701, https://doi.org/10.1029/2023MS003701, 2024.

https://doi.org/10.5194/egusphere-2026-6547
Preprint. Discussion started: 30 October 2026
© Author(s) 2026. CC BY 4.0 License.

874 Takasuka, D., Becker, T., and Bao, J.: Precipitation Characteristics and
875 Thermodynamic-Convection Coupling in Global Kilometer-Scale Simulations, J. Adv.
876 Model. Earth Syst., 18, e2025MS005343, https://doi.org/10.1029/2025MS005343, 2026.

877 Tao, W. -K., Iguchi, T., Lang, S., Li, X., Mohr, K., Matsui, T., Van Den Heever, S. C., and
878 Braun, S.: Relating Vertical Velocity and Cloud/Precipitation Properties: A Numerical Cloud
879 Ensemble Modeling Study of Tropical Convection, J. Adv. Model. Earth Syst., 14,
880 e2021MS002677, https://doi.org/10.1029/2021MS002677, 2022.

881 Tiedtke, M.: Representation of Clouds in Large-Scale Models, Mon. Weather Rev., 121,
882 3040–3061, https://doi.org/10.1175/1520-0493(1993)121%3C3040:ROCILS%3E2.0.CO;2,
883 1993.

884 Wall, C. J., Norris, J. R., Gasparini, B., Smith, W. L., Thieman, M. M., and Sourdeval, O.:
885 Observational Evidence that Radiative Heating Modifies the Life Cycle of Tropical Anvil
886 Clouds, J. Clim., 33, 8621–8640, https://doi.org/10.1175/JCLI-D-20-0204.1, 2020.

887 Waman, D., Meusel, J., Keshtgar, B., Wallentin, G., Barthlott, C., Patade, S., Shete, S.,
888 Prabhakaran, T., Fievet, R., Finney, D., Blyth, A., and Hoose, C.: Impacts of secondary ice
889 production on the microphysics and dynamics of deep convective clouds in different
890 environments, Atmos. Chem. Phys., 26, 11371–11407,
891 https://doi.org/10.5194/acp-26-11371-2026, 2026.

892 Wang, D., Prein, A., and Pothapakula, P.: Broken Environment–Storm Coupling in Global
893 Kilometer-Scale Simulations, https://doi.org/10.21203/rs.3.rs-10091203/v1, 14 July 2026.,
894 2026.

895 Wing, A. A., Reed, K. A., Satoh, M., Stevens, B., Bony, S., and Ohno, T.:
896 Radiative–convective equilibrium model intercomparison project, Geosci. Model Dev., 11,
897 793–813, https://doi.org/10.5194/gmd-11-793-2018, 2018.

898 Wing, A. A., Stauffer, C. L., Becker, T., Reed, K. A., Ahn, M., Arnold, N. P., Bony, S.,
899 Branson, M., Bryan, G. H., Chaboureau, J., De Roode, S. R., Gayatri, K., Hohenegger, C.,
900 Hu, I., Jansson, F., Jones, T. R., Khairoutdinov, M., Kim, D., Martin, Z. K., Matsugishi, S.,
901 Medeiros, B., Miura, H., Moon, Y., Müller, S. K., Ohno, T., Popp, M., Prabhakaran, T.,
902 Randall, D., Rios-Berrios, R., Rochetin, N., Roehrig, R., Romps, D. M., Ruppert, J. H.,
903 Satoh, M., Silvers, L. G., Singh, M. S., Stevens, B., Tomassini, L., van Heerwaarden, C. C.,
904 Wang, S., and Zhao, M.: Clouds and Convective Self-Aggregation in a Multimodel Ensemble
905 of Radiative-Convective Equilibrium Simulations, J. Adv. Model. Earth Syst., 12,
906 e2020MS002138, https://doi.org/10.1029/2020MS002138, 2020.